UNIVERSITY *of York*

This is a repository copy of *Novel High-Order-Harmonic Toroidal Winding Design Approach for Double-Sided Vernier Reluctance Linear Machine*.

White Rose
university consortium
Universities of Leeds, Sheffield & York

eprints@whiterose.ac.uk
https://eprints.whiterose.ac.uk/

Novel High-Order-Harmonic Toroidal Winding Design Approach for Double-Sided Vernier Reluctance Linear Machine

Zhenghao Li, Xing Zhao, Member, IEEE, Shuangxia Niu, Senior Member, IEEE

Abstract—Double-sided DC-Vernier reluctance linear machine (DS-DC-VRLM) is very suitable for long stroke industrial processing applications, taking advantages of magnet-free design, eliminated magnetic pull and high dynamic response. However, its low trust force density due to poor excitation ability of DC windings, has been a long-existing bottleneck. Aiming to boost the output thrust force of the DS-DC-VRLM, a novel high-order harmonic non-overlapped toroidal winding design is proposed. The key is that the proposed armature winding makes full use of working harmonics modulated from both fundamental order and third-order harmonics generated by DC excitations, contributing to enhanced winding factor. Based on the finite element analysis (FEA), with the proposed winding design approach, DS-DC-VRLM could achieve 2.26 times higher thrust force than those with conventional concentrated winding under the same copper loss. In this paper, new winding arrangement of DS-DC-VRLM and its operation principle are introduced, along with some design considerations of it, such as slot/pole combinations, DC/AC current distributions and extra end teeth dimensions are discussed for performance improvement. Finally, the performances of this proposed machine are evaluated by prototype experiments to verify the correctness of FEA simulation results.

Index Terms— Flux Modulation, High Order Harmonics, Long Stroke, Vernier Reluctance Linear Machine

I. INTRODUCTION

LINEAR machines have been widely used in the direct-drive applications, such as urban transit system, electromagnetic launcher and industrial processing [1-2]. Removing the gearbox and other power transmission device, linear machines take advantages of simple structure, high reliability and less mechanical loss. Meanwhile, considering the fluctuating prices of permanent magnet (PM), and its potential irreversible demagnetization problem, the PM-free linear machines have been attracting much research attention [3]. The synchronous reluctance linear machine is one of the potential non-PM candidates which has the familiar control method with that of PM synchronous linear machine. However, the drawback of this machine is that the force density of the machine is much lower than those PM-excited counterparts, and the efficiency of the machine is also too low for linear application. Other reluctance linear machines, such as the switched reluctance linear machine (SRLM) [4-5] and variable flux reluctance linear machine (VF-RLM) [6], are facing the same challenges. The research status of these reluctance linear machines is elaborated as follows. SRLM,

which benefits in the robust mechanical structure and low cost, is suitable for the long stroke linear application [4]. However, the thrust ripple of this machine is too large due to its half-period-conducting driving mode, which restricts its practical applications. To smooth the thrust ripple and simplify control method, researchers have developed primary DC-excited VF-RLM, which can basically be divided into doubly salient reluctance linear machine (DS-RLM) [7-9] and DC-excited Vernier reluctance linear machines (DC-VRLM) [10-14]. DS-RLM features a short magnetic circuit of working harmonics, which has limited thrust force density. The thrust ripple of DS-RLM is also large due to the asymmetrical magnetic circuit [7] and rich higher-order harmonics in the induced voltage [8-9]. DC-VRLM, combining Vernier machine with DC-excited machine, is an emerging non-PM candidate, and has both promising power density and robust structure.

The research on the DC-Vernier machines focus on the enhancement of output performance through the innovation of winding design, selection of slot/pole combination and application of auxiliary PM [10-15]. [11] proved that comparing with double-layer winding, single-layer armature winding possesses richer harmonics to couple with field harmonics. The reversed full DC winding machine, whose adjacent DC coils are in the reverse direction, is proposed in [12] to achieve higher gear ratio and proved to generate higher torque density than normal full-DC machine proposed in [13]. Alternative DC winding design, featuring DC coil across two slots, has been proposed as a new DC arrangement superior to the forementioned full-pitched DC winding configuration [14-15]. Comparing with full-pitched DC winding, it reduced the length of DC coil and the copper loss as well without significant compromise on output capability of the motor. Toroidal winding design, wrapping the winding on the yoke, is an effective method to shorten the ends of the coil for double-sided linear machines while avoiding reduction of thrust density, and has been applied to switched reluctance machine [16], flux reversal machine [17] and Vernier machine [18-19].

In this paper, a novel toroidal alternative single layer (TASL) winding design approach is proposed to improve the output thrust force for double-sided DC-Vernier reluctance linear machine (DS-DC-VRLM). Instead of only using the working harmonics modulated from fundamental harmonics of DC excitations, those modulated from third-order harmonics produced by the interval arrangement of DC windings can be further fully utilized with enhanced winding factors and thrust force is significantly improved accordingly. Meanwhile, with the proposed winding design, the end windings are shortened, copper loss is reduced, and hence the efficiency of the motor is improved.

The rest of paper is organized as follows. In Section II, the machine structure, the winding configuration are introduced, and the operation principle of the proposed winding are studied using the harmonics analysis. In Section III, the parametric model of the linear machine is investigated and Multi-objective Genetic Algorithm (MOGA) is also carried out to optimize the geometric dimensions of the machines with different slot/pole combinations. In Section IV, the optimal cases with different slot/ pole combination are comprehensively compared in terms of their no-load performances, thrust force, loss and efficiency performances. In Section V, a prototype is fabricated, and the experiments are performed for the feasibility verification of proposed solution. Finally, some conclusions are drawn in Section VI.

II. OPERATION PRINCIPLE

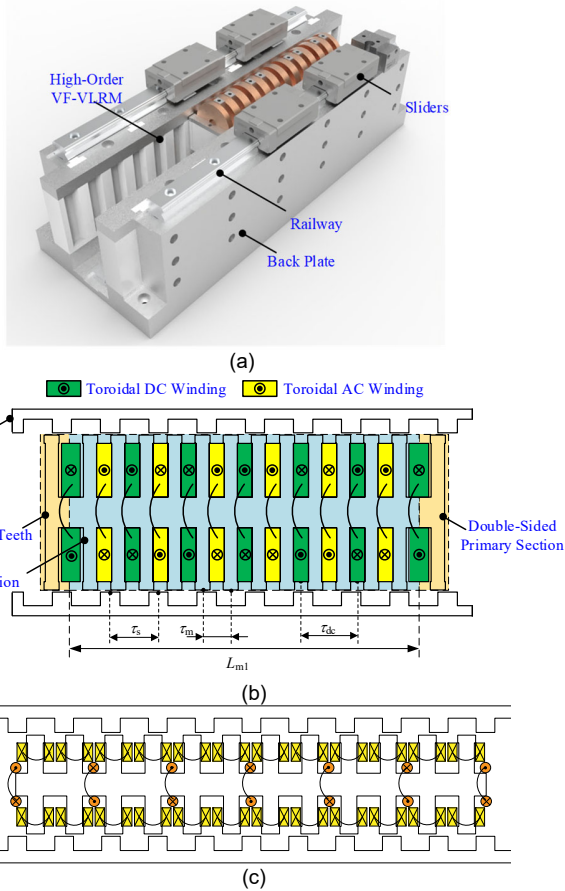### A. Machine Structure and Toroidal Winding Design

Fig. 1. Sketch of the proposed machine. *(a) 3D model (b)Cross section. (c) Cross section of conventional design*

Fig. 1(a) depicts 3D model of the proposed double-sided DC-Vernier reluctance linear machine (DS-DC-VRLM) and Fig. 1(b) demonstrates the cross section of it. From perspective of the primary part, it adopts double-sided structure and toroidal winding configuration. There are 12 primary slots each side housing two group windings in the effective part, namely DC field winding and armature windings, respectively, which are wound toroidally on the yoke. The secondary stators adopt salient-pole teeth to construct a doubly-salient structure locate on both side of the mover symmetrically, which is relatively low-cost and obtains good robustness meanwhile. Fig. 1(c) illustrates the conventional concentrated double layer (DL) winding. Both

of the two machines employ the same alternatively-toroidal-wound DC field winding [14] [21].
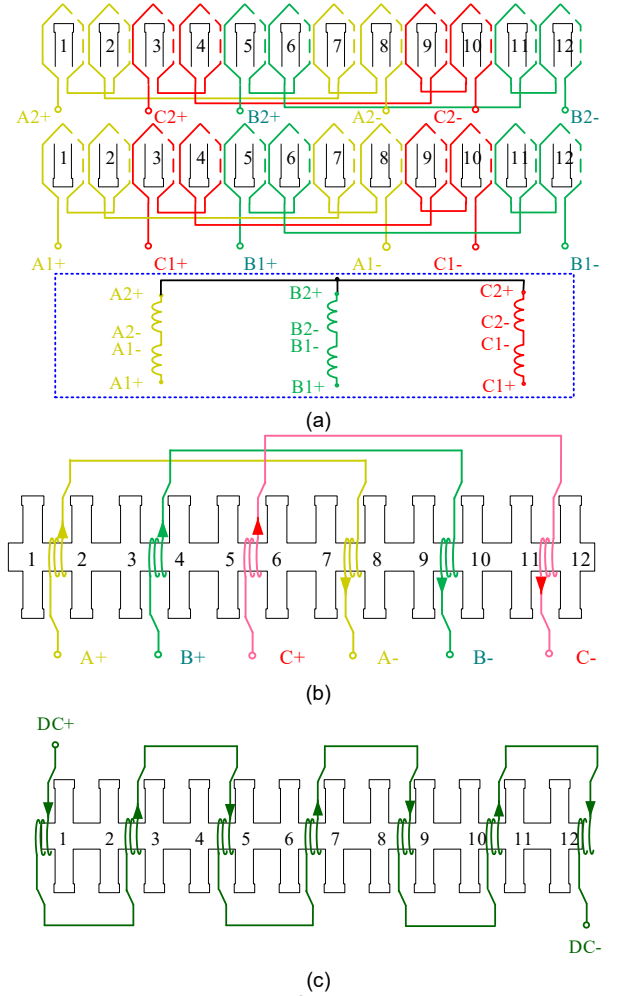

Fig. 2. Winding connections. *(a) Conventional concentrated windings. (b) Armature winding of proposed TASL windings. (c) DC field winding arrangement.*

Some geometric parameters are denoted in Fig. 1(b). It is shown in Fig.1 (b) that the DC field winding is wound toroidally every two primary teeth, and the direction of adjacent DC windings is opposite to each other, which generates much richer harmonics. Through doing this, the fundamental pole pair number (*PPN*) of DC excitation, denoted as P_{dc}, can be calculated as (1),

$$P_{dc} = \frac{N_m}{4} \qquad (1)$$

where N_m is the number of effective parts of mover slots (N_m=12). On the basis of the flux modulation theory, the main working harmonics is generated by fundamental harmonics and modulated by salient-pole teeth of secondary, whose *PPN* could be calculated as (2). The conventional concentrated double layer (DL) windings designed following (2) and only utilizing the fundamental working harmonics is shown in Fig. 2(a),

$$P_w = |P_{dc} - N_s| \qquad (2)$$

where N_s is the number of secondary teeth aligned with mover.

On the other hand, considering the interval arrangement of DC excitation, based on the flux modulation theory, other working harmonics are generated by higher-order harmonics, especially the 3rd harmonics, whose *PPN* could be calculated as (3). The proposed toroidal alternative single layer (TASL) windings,

which are wound toroidally every two teeth, are designed to utilize harmonic in (3) and shown in Fig. 2(b),

$$P'_w = |3P_{dc} - N_s| \qquad (3)$$

Fig. 2(c) presents the winding configuration of DC coils. As shown in Fig. 2(c), the coils of DC winding are wound toroidally on the yoke of the mover, which are distributed alternatively in the mover slots. The interval arrangement of DC windings is an emerging DC arrangement which could achieve comparable excitations with reduced DC coils and associated power loss.

B. Flux Density Distributions of DC Excitation

From the perspective of DC excitation, the magnetomotive force (MMF) excited by DC field winding, denoted as $F_{dc}(x)$, can be regarded as square waveform with translation displacements. The definitions regarding to the DC excitation have been denoted in Fig. 1(b). The Fourier series expansion of its MMF can be Further expressed as follows,

$$\begin{cases} F_{dc}(x) = \sum_{h=1,3,5\dots} \frac{4F_{max}}{h\pi} \sin\left(\frac{h\pi}{\tau_{dc}} x\right) \\ F_{max} = N_{dc} I_{dc} \end{cases} \qquad (4)$$

where F_{max} is the maximum value of MMF of the DC windings, h is the order of the MMF harmonics, and τ_{dc} is the distance between two adjacent DC coils.

The MMF of DC excitation F_{DC} is firstly modulated by mover teeth, whose normalized permeance function $\Lambda_m(x)$ can be expressed as follows,

$$\begin{cases} \Lambda_m(x) = \Lambda_{m_{(0)}} + \sum_{n_1=1,2,3\dots} \Lambda_{m_{(n_1)}} \cos\left(\frac{2n_1\pi}{\tau_m} x\right) \\ \Lambda_{m_0} = \frac{2\Lambda_m x_1}{\tau_m} \\ \Lambda_{m_{n_1}} = \frac{2\Lambda_m}{n_1\pi} \sin\left(\frac{n_1\pi}{\tau_m} x_1\right) \end{cases} \qquad (5)$$

where n_1 is the order of normalized mover permeance function $\Lambda_m(x)$, τ_m is the distance between two adjacent mover teeth ($\tau_m = \frac{\tau_{dc}}{2}$) and x_1 is the width of the mover slot. $\Lambda_{m(min)}$ and $\Lambda_{m(max)}$ are minimum and maximum values of the permeance coefficient. Modulated by the mover teeth, the MMF of DC excitation is modified, denoted as $F'_{dc}(x)$. Fig. 3 illustrated the MMF of DC excitation (blue dash line), and the modified MMFs of it (red line) after being modulated by mover teeth. By substituting (4) and (5), $F'_{dc}(x)$ is expressed as (6),

$$F'_{dc}(x) = F_{DC} \cdot \Lambda_m = \sum_{h=1,3,5\dots} \frac{4F_{max}}{h\pi} \sin\left(\frac{h\pi}{\tau_{dc}} x\right) \qquad (6)$$

$$\cdot \left[\Lambda_{m0} + \sum_{n=1,2,3\dots} \Lambda_{m_{n_1}} \cos\left(\frac{2n_1\pi}{\tau_m} x\right)\right]$$

$$= \sum_{h=1,3,5\dots} \sum_{n_1=0,1,2\dots} \frac{2F_{max}}{h\pi} \Lambda_{m_{n_1}} \sin\left[(h \pm 4n_1)\frac{\pi}{\tau_{dc}} x\right]$$
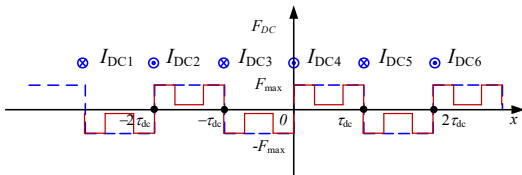

Fig.3. MMF generated by DC excitation.

Therefore, modulated by mover teeth, the *PPN* of the higher-order MMF of DC excitations could be calculated as,

$$P'_{dc} = (h \pm 4n_1)P_{dc} \qquad (7)$$

when h=1, and n_1=1, DC winding produced the 3rd order and 5th order harmonics in the air gap. As 5th order harmonics attenuate fast in the air gap, (7) indicates that 3rd order harmonics might be utilized as new set of feasible working harmonics besides fundamental harmonics (h=1, and n_1=0).

Meanwhile, the permeance function of the secondary stator aligning with the mover $\Lambda_s(x, t)$ can be expressed as a set of Fourier series in (8). To facilitate the calculation process, the mover is setting as stationary, and the speed of secondary stator part is set as -v_m. Therefore, the permanence function of the stator can be expressed as follows,

$$\begin{cases} \Lambda_s(x,t) = \Lambda_{s_0} + \sum_{n_2=1,2,3\dots} \Lambda_{s_{n_2}} \cos\left[\frac{2n_2\pi}{\tau_s}(x + v_m t)\right] \\ \Lambda_{s_0} = \frac{2\Lambda_s x_2}{\tau_s} \\ \Lambda_{s_{n_2}} = \frac{2\Lambda_s}{n_2\pi} \sin\left(\frac{n_2\pi}{\tau_s} x_2\right) \end{cases} \qquad (8)$$

where $\Lambda_{s(n2)}$ is the amplitude of n_2th order harmonics of stator permeance function, τ_s is the pole pitch of the stator teeth, x_2 is the width of stator slot, $\Lambda_{s(min)}$ and $\Lambda_{s(max)}$ are the minimum and the maximum value of it. The field density can be deduced by the product of $F'_{dc}(x)$ and the permanence function of the secondary stator $\Lambda_s(x,t)$, which is expressed as (9).

$$B_{(h,n1,n2)}(x,t) = F'_{dc}(x) \cdot \Lambda_s(x,t) \qquad (9)$$

$$= \sum_{h=1,3,5\dots} \sum_{n1=0,1,2\dots} \frac{2F_{max}}{h\pi} \sin\left((h \pm 4n_1)\frac{\pi}{\tau_{dc}} x\right) \cdot \Lambda_{m_{n1}}$$

$$\cdot \sum_{n_2=1,2,3\dots} \Lambda_{s0} + \Lambda_{s_{n2}} \cos\left[\frac{2n_2\pi}{\tau_s}(x + v_m t)\right]$$

$$= \sum_{n_2=0,1,2\dots} \sum_{h=1,3,5\dots} \sum_{n1=0,1,2\dots} \frac{F_{max}}{h\pi} \Lambda_{m_{n_1}} \Lambda_{s_{n_2}}$$

$$\cdot \sin\left\{\frac{2\pi}{L_{m1}} \left[((h \pm 4n_1)P_{dc} \pm n_2 N_s)(x + \frac{n_2 N_s}{(h \pm 4n_1)P_{dc} \pm n_2 N_s} v_m t)\right]\right\}$$

To be noticed, the *PPN* of main working harmonics generated by DC excitations could be summarized by (10),

$$P_w = |(h \pm 4n_1)P_{dc} - N_s| \qquad (10)$$

TABLE I HARMONICS OF FLUX DENSITY IN AIR-GAP

	Spatial Order	Amplitude	Speed
I	hP_{dc}	$\frac{4\mu_0 F_{max}}{gh\pi} \Lambda_{m_{(0)}} \Lambda_{s_{(0)}}$	0
II	$(h \pm 4n_1)P_{dc}$	$\frac{2\mu_0 F_{max}}{gh\pi} \Lambda_{m_{(n1)}} \Lambda_{s_{(0)}}$	0
III	$(h \pm 4n_1)P_{dc} \pm n_2 N_s$	$\frac{\mu_0 F_{max}}{gh\pi} \Lambda_{m_{n1}} \Lambda_{s_{n2}}$	$\frac{n_2 N_s}{(h \pm 4n_1)P_{dc} \pm n_2 N_s} v_m$

According to the analysis above, the flux density in the airgap can be fully expanded and summarized in TABLE I. Basically, the harmonics in the airgap generated by DC windings are comprised of three groups. Group I is generated by DC excitation without any modulation effect. Group II is generated only by mover teeth modulation effect. Group III is modulated by both the mover and stator teeth. It should be noticed that harmonics in Group I and II are stationary, while those in Group III are in motion and could serve as working harmonics to produce thrust force.

C. Working harmonics contribution comparison

According to (7) and (10), the working harmonics of the proposed winding arrangement could be selected from the components modulated by both fundamental *PPN* of DC excitation P_{dc} (h=1, n_1=0) and higher-order *PPN* of it P'_{dc} (h=1,

n_1=1). Substituting (5) and (8) into (9), the amplitudes comparison of these two sets of working harmonics could be calculated as (11),

$$\left|\frac{B_{(1,0,1)}}{B_{(1,1,1)}}\right| = \left|\frac{\frac{2F_{max}}{h\pi}\Lambda_{m_0}\Lambda_{s_1}}{\frac{F_{max}}{h\pi}\Lambda_{m_1}\Lambda_{s_1}}\right| = \left|\frac{2\Lambda_{m_0}}{\Lambda_{m_1}}\right| = \left|\frac{\Lambda_{m(max)}+\Lambda_{m(min)}}{\frac{2}{\pi}(\Lambda_{m(max)}-\Lambda_{m(min)})\sin\left(\frac{\pi}{\tau_m}x_1\right)}\right|$$
(11)

When we assume that 1) Based on the calculation results of equation (5) and (8), the ratio between the maximum value of permeance function $\Lambda_{m(max)}$ and minimum value of permeance function $\Lambda_{m(min)}$ should be 10:1. 2) the width of the mover slot x_1 is equal to half of the mover teeth pole pitch τ_m, that is, x_1=1/2 τ_m. Therefore, substituting (5) into (11), the amplitudes comparison of these two sets of working harmonics could be calculated as following (12),

$$\left|\frac{B_{(1,0,1)}}{B_{(1,1,1)}}\right| = \frac{11}{9} \times \frac{\pi}{2} \approx 1.92$$
(12)

Based on the assumptions above, the calculation results indicate that the amplitude of component modulated by fundamental *PPN* of DC excitation is approximately 92% higher than that of component modulated by higher-order *PPN* of DC excitation P'_{dc}.

On the other hand, mechanical velocity of the working harmonics is another factor affecting the contribution of the harmonics, which could be calculated as (13),

$$v_{mec} = G_r v_m = \frac{N_s}{(h\pm 4n_1)P_{dc}\pm n_2 N_s} v_m$$
(13)

where v_{mec} is the mechanical speed of the working harmonics, G_r is the gear ratio of the harmonics, and N_s is the number of stator teeth. As shown in (13), the lower order of the working harmonics, the higher mechanical speed could be achieved. Thereafter, even though the amplitude of working harmonics modulated from fundamental harmonics of DC excitation P_{dc} are higher than those modulated from 3rd order harmonics P'_{dc}, the latter could also be utilized and make contribution to the enhanced induced voltage and higher output thrust when the components have higher mechanical speed and gear ratio. Therefore, the harmonics modulated from 3rd order harmonics P'_{dc}, may also be selected as working harmonics, and provide new feasible harmonics to generate the thrust force for the proposed linear machine.

To make full use of the working harmonics modulated by P'_{dc}, the TASL winding is connected following the equation (3) and (10). The winding function $N_a(x)$ is defined as the MMF of one phase armature winding at unit current, which can be expressed by (14), when the origin point is aligned with the middle point of the armature winding slot [17],

$$N_a(x) = \sum_{j=1,3,5\cdots} \frac{2}{\pi}\frac{1}{jP_{ac}}T_{ac}k_{wj}\sin\left(j\frac{\pi}{\tau_{ac}}x\right)$$
(14)

where j is the order of the armature winding function harmonics, P_{ac} is the fundamental *PPN* of armature winding, and equals to $|3P_{dc}-N_s|$, T_{ac} is the turns of armature winding, k_{wj} is the winding factor of the jth order harmonics, and τ_{ac} is the pole pitch of armature winding.

According to winding function theory, the flux linkages can be expressed as (15),

$$\psi_m(t) = 2\psi_{m1}(t) = 2l_{stk}\int_0^{L_x} B_{(h,n1,n2)}(x,t)\cdot N_a(x)dx \quad (15)$$

$$= \frac{2}{\pi}l_{stk}T_{ac}B_{(h,n1,n2)}k_{wn}\tau_w\cos\left(\frac{2\pi}{L_x}n_2 N_s v_m t\right)$$

The major factors determining the amplitude of flux linkages in the armature winding can be classified into four categories, which are: 1) geometric dimensions such as stack length l_{stk}, 2) τ_w, 3) field densities parameters, such as $B_{(h,n1,n2)}$, 4) armature winding configuration, such as winding function k_{wn} and T_{ac}. The winding factors k_{wn} can be calculated as (16),

$$\begin{cases} k_{wn} = k_{pn}k_{dn} \\ k_{pn} = \sin\frac{\tau_{ac}}{\tau_w}\frac{\pi}{2}, k_{dn} = \frac{\sin\left(qn\frac{\alpha}{2}\right)}{q\sin\left(n\frac{\alpha}{2}\right)} \end{cases}$$
(16)

where q is the number of the coil per phase under the same phase, τ_w is the pole pitch of working harmonics and α is the phasor differences between the neighboring coils.

Therefore, the open-circuit induced voltage of one phase of TASL winding can be calculated as following (17),

$$e_m(t) = -\frac{d\psi_m(t)}{dt}$$
(17)

$$= 2l_{stk}B_{(h,n1,n2)}k_{wn}G_r v_m \sin\left(\frac{2\pi}{L_x}n_2 N_s v_m t\right)$$
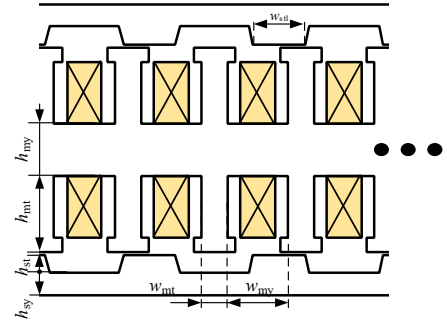
D. Flux Calculation and Winding Harmonics Analysis

Fig.4. Geometric parameters of VF-VRLM

TABLE II DESIGN PARAMETER OF THE EXAMPLE

Symbol	Parameter	unit	Prop. Design	Conv. Design
H_{total}	Total length along Y-axis	mm	80	
k_{sp}	Split ratio	-	0.7	
h_{mt}	Height of mover teeth	mm	30	
h_{st}	Height of stator teeth	mm	6.5	
L_m	Mover length	mm	210	
k_{st}	Ratio of stator teeth width	-	0.5	
N_{dc}	Number of dc coil turns	-	100	
N_{ac}	Number of ac coil turns	-	100	50
N_{coil}	Number of ac coils	-	2	4
J_e	Current density	A/cm2	600	
v_m	Velocity	m/s	1	

The main design parameters of the proposed machine are defined in Fig. 4, and the geometric dimensions for the initial design examples are listed in the Table II. Fig. 5 takes machine with 12 slots as an example, and the waveforms and the spectrums of the flux densities of machines with all feasible slot/pole combinations 12/5, 12/7, 12/8 12/10 and 12/11 in the air-gap are presented. The components modulated by third-order *PPN* of DC excitation P'_{dc} are denoted with blue color, and the components modulated by fundamental harmonics of DC excitation P_{dc} are denoted with red color. As shown in Fig. 5, the *PPN*s of main working harmonics generated by fundamental harmonics P_{dc} are 2 for 12/5 case, 4 for 12/7 case, 5 for 12/8 case and 7 for 12/10 case. On the other hand, the *PPN*s of main working harmonics generated from 3rd order harmonics P'_{dc} are 4 for 12/5 case, 2 for 12/7case and 12/11 case, 1 for 12/8 and 12/10 cases, respectively.

TABLE IV INDUCED VOLTAGE GENERATION OF PROPOSED TASL WINDING WITH 12/8 SLOT POLE COMBINATION

P'_{dc}	P_s	(h,n_1,n_2)	P_{ac}	T_{ac}	P_w	τ_w	τ_s	G_r	$B_{h,n}$	k_{pn}	k_{dn}	v_m	$E_{ph1}(*)$	$|\Sigma E_{ph1}|$	FEA
9	8	(1,0,-1)	1	1	5	1.20	0.75	1.6	0.0874	1	1	1	8.39	27.34	34.70
		(1,-1,-1)			1	6.00		8	0.0472	1	1	1	22.66		
		(1,1,-1)			7	0.86		1.14	0.0133	-1	1	1	-0.91		
		(1,-2,-1)			13	0.46		0.62	0.0049	1	1	1	0.18		
		(1,2,-1)			19	0.32		0.42	0.0158	-1	1	1	-0.40		
		(1,-3,-1)			25	0.24		0.32	0.0089	1	1	1	0.17		
		(1,3,1)			31	0.19		0.26	0.0030	-1	1	1	-0.05		
		(1,0,1)			11	0.55		0.73	0.0861	-1	1	1	-3.76		
		(1,-1,1)			17	0.35		0.47	0.0504	1	1	1	1.42		
		(1,1,1)			23	0.26		0.35	0.0169	-1	1	1	-0.35		
		(1,-2,1)			29	0.21		0.28	0.0006	1	1	1	0.01		
		(1,2,1)			35	0.17		0.23	0.0023	-1	1	1	-0.03		
		(1,-3,1)			41	0.07		0.20	0.0019	1	1	1	0.02		
		(1,3,1)			47	0.06		0.17	0.0016	-1	1	1	-0.02		

TABLE V INDUCED VOLTAGE GENERATION OF CONVENTIONAL WINDING WITH 12/8 SLOT POLE COMBINATION

P_{dc}	P_s	(h,n_1,n_2)	P_{ac}	T_{ac}	P_w	τ_w	τ_s	G_r	$B_{h,n}$	k_{pn}	k_{dn}	v_m	$E_{ph1}(*)$	$|\Sigma E_{ph1}|$	FEA
3	8	(1,0,-1)	1	1	5	1.20	0.75	1.6	0.0874	0.97	1	1	8.10	7.26	8.83
		(1,-1,-1)			1	6.00		8	0.0472	0.26	0	1	0.00		
		(1,1,-1)			7	0.86		1.14	0.0133	0.97	1	1	0.88		
		(1,-2,-1)			13	0.46		0.62	0.0049	-0.26	0	1	0.00		
		(1,2,-1)			19	0.32		0.42	0.0158	-0.97	1	1	-0.39		
		(1,-3,-1)			25	0.24		0.32	0.0089	0.26	0	1	0.00		
		(1,3,1)			31	0.19		0.26	0.0030	0.97	1	1	0.05		
		(1,0,1)			11	0.55		0.73	0.0861	0.26	0	1	0.00		
		(1,-1,1)			17	0.35		0.47	0.0504	-0.97	1	1	-1.37		
		(1,1,1)			23	0.26		0.35	0.0169	-0.26	0	1	0.00		
		(1,-2,1)			29	0.21		0.28	0.0006	0.97	1	1	0.01		
		(1,2,1)			35	0.17		0.23	0.0023	0.26	0	1	0.00		
		(1,-3,1)			41	0.07		0.20	0.0019	-0.97	1	1	-0.02		
		(1,3,1)			47	0.06		0.17	0.0016	-0.26	0	1	0.00		

The amplitudes of the main working harmonics $B_{(h,n_1,n_2)}$ and gear ratio G_r of the two harmonics are listed in Table III. According to TABLE III, $B_{(1, 0, -1)}$ has higher amplitudes than those of $B_{(1, 1, -1)}$, whose ratios are 1.69 for 12/5 case, 1.57 for 12/7 case, 1.85 for 12/8 case, 1.88 for 12/10 case and 1.58 for 12/11 case, respectively, which basically agree with the theoretical value calculated in (12). However, except for 12/5 case, the gear ratios of $B_{(1, 1, -1)}$ are much higher than $B_{(1, 0, -1)}$, the ratios between G_r of $B_{(1, 1, -1)}$ and $B_{(1, 0, -1)}$ are 2 for 12/7 case, 5 for 12/8 case, 7 for 12/10 case and 4 for 12/11 case, indicating that harmonic $B_{(1, 1, -1)}$ could contribute more to induced voltage than $B_{(1, 0, -1)}$.
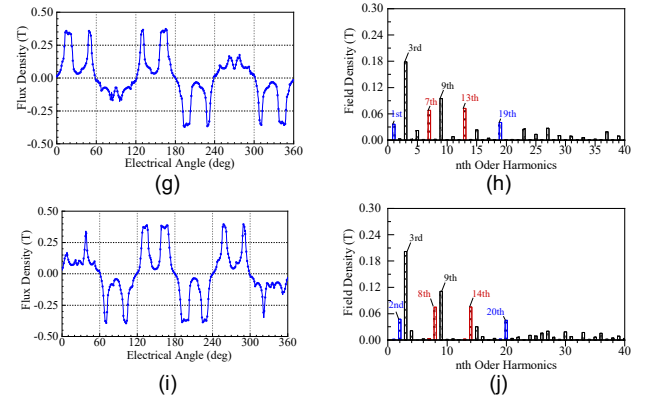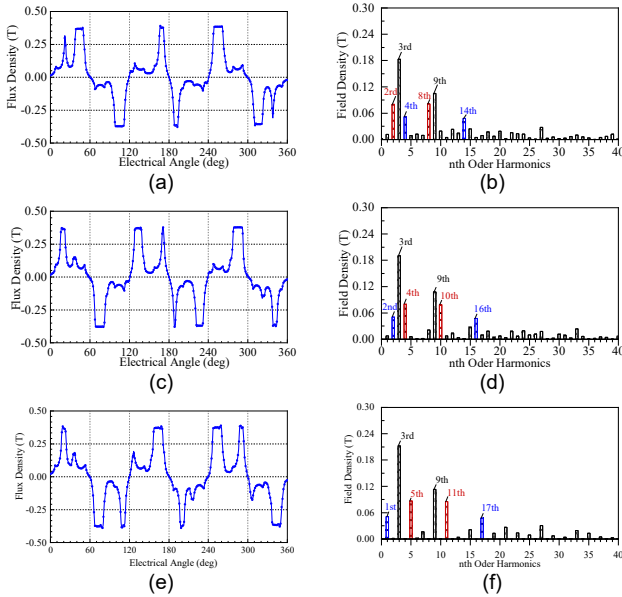

Fig. 5 DC-excited flux density. *(a) 12-5 waveforms. (b) 12-5 spectrum. (c) 12-7 waveforms. (d) 12-7 spectrum. (e) 12-8 waveforms. (f) 12-8 spectrum. (g) 12-10 waveforms. (h) 12-10 spectrum. (i) 12-11 waveforms. (j) 12-11 spectrum.*

TABLE III COMPARISON OF DIFFERENT WORKING HARMONICS

	$B_{(1, 0, -1)}$	$B_{(1, 1, -1)}$	$\dfrac{B_{(1,0,-1)}}{B_{(1,1,-1)}}$	$G_{r(1, 0, -1)}$	$G_{r(1, 1, -1)}$	$\dfrac{G_{r(1,1,-1)}}{G_{r(1,0-1)}}$
12/5	0.0819	0.0484	1.69	2.5	1.25	0.5
12/7	0.0800	0.0508	1.57	1.75	3.5	2
12/8	0.0874	0.0472	1.85	1.60	8	5
12/10	0.0681	0.0363	1.88	1.43	10	7
12/11	0.0749	0.0473	1.58	1.36	5.5	4

Following the design parameters listed in TABLE II, the induced voltages of the two winding configurations of feasible slot/pole combinations are calculated at unit speed under the same DC field excitation via analytical and FEA methods. The contributions of different harmonics to the induced voltages are calculated quantitatively via equation (17), the results of 12/8 design are taken as an example and listed in TABLE IV and V.

According to TABLE IV and V, TASL winding could achieve higher induced voltage than conventional windings. This is because TASL makes full use of both components modulated by 3rd-order harmonics of DC excitation P'_{dc} as well as the components modulated by fundamental harmonics P_{dc}. Compared with conventional winding, it possesses richer harmonics to couple with the higher order harmonics. In addition, TASL winding obtains higher harmonics winding factors, which is also superior to conventional concentrated double layer winding.

TABLE VI compared the fundamental components of induced voltage in each phase calculated by analytical and FEM methods, where the errors of two methods are provided. In specific, the proposed TASL could achieve 93.47% higher induced voltage for 12/5 case, 81.47% for 12/7 case, 91.19% for 12/8 case, 49.82% for 12/10 case, and 66.64% for 12/11 case than conventional concentrated windings. However, if the number of poles increases further, the superiority of TASL is apparently no longer obvious, which is because the yoke flux is effectively reduced due to the flux leakages caused by increasing number of teeth. The calculation errors between the analytical and FEA methods are also provided in the table.

TABLE VI INDUCED VOLTAGES OF PROPOSED ARMATURE WINDING

Slot/Pole	Analytical (TASL)	FEA (TASL)	Analytical (Conv.)	FEA (Conv.)	Ratio (Anal.)	Ratio (FEA.)	Error (%)
12/5	47.66	45.66	22.12	23.60	2.15	1.93	9.30
12/7	55.36	51.90	28.08	28.60	1.97	1.83	7.10
12/8	54.68	67.56	29.04	35.32	1.88	1.91	1.51
12/10	40.78	33.56	28.28	22.40	1.44	1.49	3.36
12/11	49.12	46.06	27.48	27.64	1.77	1.66	6.21

III. MACHINE DESIGN MECHANISM

Some design guidelines of the linear machine, including the impacts of some key parameters, are studied in this section. Meanwhile, a multi-objective optimization algorithm is set up to optimize the key parameters to improve the performance.

A. Parametric Analysis

The impact of the split ratio k_{sp}, which is defined as the ratio between the height of the mover and the machine, the DC loss ratio k_{dc} and the ratio of width of stator teeth and mover teeth k_{sm} are investigated. The split ratio k_{sp} is defined as (18),

$$k_{sp} = \frac{h_m}{H_{total}} \qquad (18)$$

where h_m is the height of mover part, H_{total} is the height of the total machine. Fig. 6 investigates the influence of split ratio k_{sp} and stator yoke height h_{sy} on the output thrust and force ripple.

According to Fig. 6(a) when the mover yoke height increases from 2 to 5, the output thrust increase as the saturation in the yoke is relieved. However, when the yoke height increases further, the space for field and armature winding is suppressed which decreases the output thrust. The optimized value of split ratio k_{sp} is around 0.67. When k_{sp} is lower than this value, the output thrust of the proposed DC-VRLM shows a distinct increase as the k_{sp} increases. This is because larger mover provides more space for DC and AC windings, and the magnetic and electrical load of the machine are also boosted. However, when the k_{sp} increases furtherly, the output thrust force decreases meanwhile. This is because the height of stator yoke h_{sy} is suppressed, which makes the stator easy to saturate.

Meanwhile, DC loss ratio is defined as follows,

$$k_{dc} = \frac{p_{dc}}{p_{cu}} \qquad (19)$$

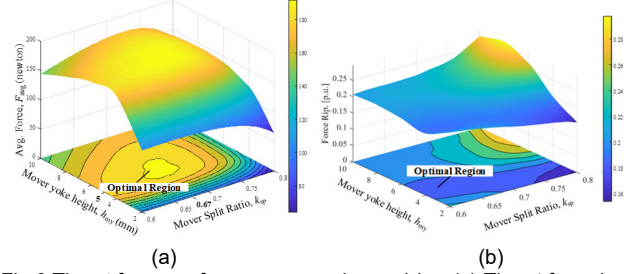where p_{dc} is the copper loss of DC current, and p_{cu} is the total copper loss of the machine.

Fig.6 Thrust force performances v.s. h_{my} and k_{sp}. *(a) Thrust force in average. (b) Thrust force ripple.*
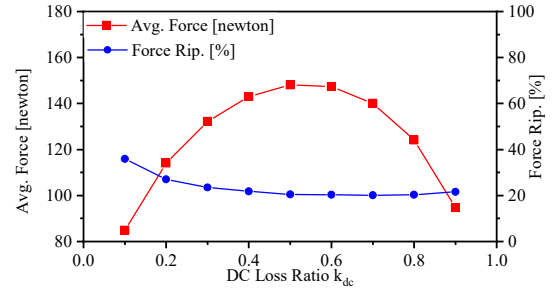

Fig.7. Thrust force performances v.s. DC loss ratio

Fig.7 indicates the influence of DC power loss ratio k_{dc}. The optimized value of k_{dc} is approximately 0.5~0.6. This is because the proposed high-order VF-VRLM achieve highest thrust force when the electrical load and magnetic load are in balance. Because of the end effect of the linear machine, the power loss of the DC windings is a little bit greater than that of AC windings. DC loss ratio shows little influence on the thrust ripple since the thrust force ripple of the machine are almost unchanged.
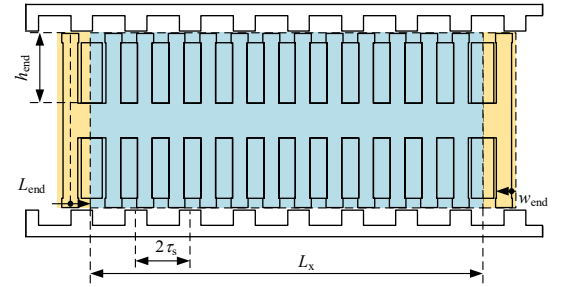

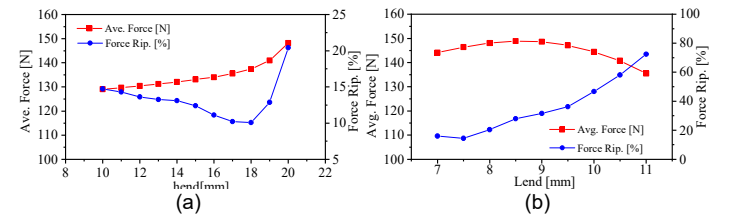Fig. 8. Geometric dimensions of auxiliary teeth.

Fig. 9. Influence of the parameters of auxiliary teeth. (a) h_{end}. (b) L_{end}

To relieve the end effect, the extra teeth are added at the front and back end of the proposed machine, as shown in Fig. 8. the length and height of the extra teeth, L_{end} and h_{end}, are used to depicts the dimensions of the extra teeth.

It can be found in Fig. 9 (a) that as h_{end} increases, the output thrust increases as well, which can be attributed to the decrease of effective air-gap length. However, when the effective air-gap length decreases furtherly, the thrust ripple of the machine is inevitably boosted. Therefore, the optimized result for h_{end} is slightly smaller than that of normal teeth. According to Fig. 9 (b), when the length of end teeth increases, the thrust force initially increases. As the length of auxiliary teeth rises up, more space is available for the DC winding at ends. However, as the further increase of L_{end} unavoidably amplifies the reluctance of the magnetic path, the thrust force will then decrease.

B. Global Optimization

In this section, machines with 12-7 and 12-8, which achieve relatively better thrust force performance, are optimized in detail furtherly. Machines with conventional concentrated windings are also taken into consideration for comparison. For fair comparison, the motors with different feasible slot/pole combinations and winding configurations are compared under the same copper loss (240W), volume (0.84L), length of air gap (1mm), filling factor F_f, etc., which are listed in Table VII.

The parameters of the proposed DS-DC-VRLM, including k_{sp}, k_{dc}, k_{sm}, w_{st}, h_{end} and L_{end}, are optimized globally via multi-objective genetic algorithm (MOGA). The optimization method used in this paper combined the MOGA with finite element method to search the optimal design parameters. The maximum generation is set as 40 with 30 individuals in each generation. The average output thrust force and force ripple ratio are selected as two objective functions.

TABLE VII FIXED PARAMETERS FOR COMPARISON

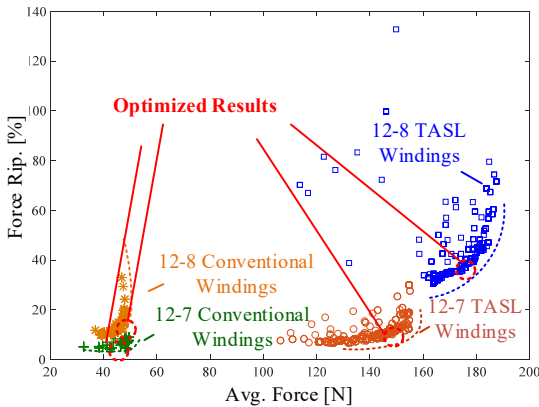| Symbol	Parameter	unit	Value
g	Air-gap length	mm	1
L_x	Mover length	mm	210
H_{total}	Total length along Y-axis	mm	80
L_{st}	Stack Length	mm	50
P_{loss}	Total loss of AC and DC	W	240
F_f	Filling factor	-	0.4

Fig. 10. Optimized Pareto front.

The optimized Pareto Front indicating the optimization results of the last generation are illustrated in the Fig.10. According to optimized Pareto front shown in Fig. 10 and TABLE VIII, machines with 12/8 design could achieve higher output thrust than its 12/7 counterpart in both proposed TASL winding and conventional double-layer concentrated winding. However, due to the lower detent force and even-order harmonics in the induced voltage, 12/7 design takes advantages of lower thrust ripple. To

be more specific, the thrust ripple of 12/7 design with TASL winding could be reduced to as low as 7.76%, and 5.42% with conventional double-layer concentrated winding. Considering the trade-off between output thrust force and thrust ripple, the optimized designs are picked up, and the parameters of them are listed in Table VIII. Comparing with machines with conventional concentrated winding, the proposed machine with TASL winding could achieve 226% higher thrust force thanks to the richer working harmonics and more enhanced winding factors.

TABLE VIII OPTIMIZED PARAMETERS AND PERFORMANCES COMPARISON

	TASL		Conv. Winding	
Parameter	12/7	12/8	12/7	12/8
w_{st}, Width of stator teeth (mm)	8.4	9.7	14.4	11.3
h_{my}, Mover yoke height (mm)	10.8	17	11.8	12
h_{sy}, Stator yoke height (mm)	5	6.4	7.3	6.7
h_{end}, End height (mm)	19.80	19.80	-	-
L_{end}, End length (mm)	8.35	7.10	-	-
w_{end}, End teeth width (mm)	2	0.2	-	-
k_{sp}, Split ratio	0.71	0.71	0.73	0.73
k_{dc}, DC to total loss ratio	0.54	0.66	0.45	0.43
N_{ac}, Number of AC turns per coil	86	70	68	76
N_{dc}, Number of DC turns per coil	86	70	56	57
R_{ac}, Resistance per phase (Ω)	0.485	0.393	0.386	0.427
i_{dc}, DC Current (A)	10.13	12.84	10.67	10.33
i_q, Q-axis RMS Current (A)	8.71	8.32	10.67	10.33
f_t, Rated thrust force (N)	154.50	174.50	47.40	50.30
f_d, Detent force (N)	3.90	44.14	2.02	9.92
f_{rip}, Force ripple (%)	11.12	37.13	11.03	29.54
D_d, Thrust force density(kN/m^3)	178.98	202.15	54.91	58.27

IV. MACHINE ELECTROMAGNETIC PERFORMANCE ANALYSIS
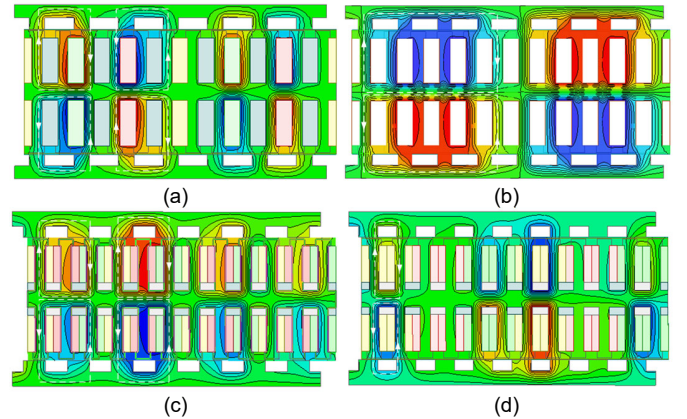
A. Flux Distributions

Fig. 11 Flux densities distributions of two windings. *(a) Proposed TASL with 12s/7p. (b) Proposed TASL with 12s/8p. (c) Concentrated winding with 12s/7p. (d) Concentrated winding with 12s/8p.*

Due to the same DC winding arrangements, Fig. 11 presents the flux densities of the armature windings of the TASL winding and conventional concentrated winding for comparison. By comparison, proposed TASL winding has lower order harmonics with longer magnetic path, which are 2nd order for 12-7 and 1st order for 12-8 design. However, concentrated DL winding generates field density with higher order, which are 4th order for 12-7 design and 5th order for 12-8 design.

B. Open-Circuit Performances

Fig. 12 presents the induced voltage of the proposed motors. Similarly, TASL boosts the fundamental components, which reaches 8.34V for 12/7 cases and 11.26V for 12/8 cases. To be

noted, the proposed winding configuration causes more high-order harmonics whose total harmonic distortion (THD), equals to 24.64% for 12/7 and 8.96% for 12/8 which may cause higher thrust force ripple. Fig. 13 compares the detent forces of the proposed motors, and their conventional winding counterparts. As shown in Fig. 13(a), The amplitude of detent force is 1.45N for TASL 12/7 design and 16.61N for 12/8 design, which is mainly attributed to the low frequency of cogging force of 12/8 design. The large detent force also accounts for the large force fluctuations of 12/8 design.
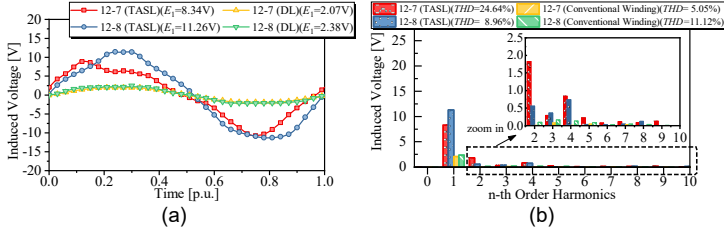
Fig. 12 Induced voltages of two windings. *(a) Proposed TASL winding and conventional winding waveforms. (b) Proposed TASL winding and conventional winding spectrums.*
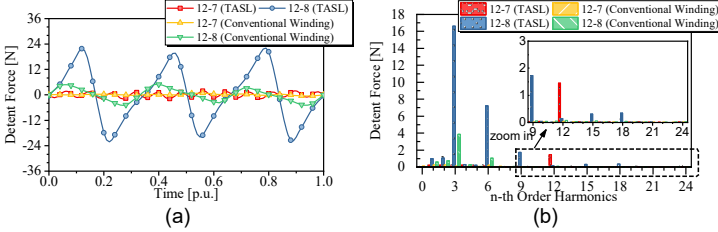

Fig. 13. Detent force of the two winding configurations. *(a) Waveforms of the detent forces. (b) Spectrum of the detent forces.*

C. Thrust Force Analysis

Fig. 14 demonstrates the thrust characteristics of the proposed machine under different copper loss with the same optimal k_{dc}. As shown in Fig. 14(a), when the electrical load increases to 1.5 times of the rated value, machine with TASL gradually reaches saturation state, and the ratio of output thrust between TASL and Conv. winding has declines from 2.47 to 1.86. The force ripple of 12/8 design is over 30%, which is much higher than its 12/7 counterpart in both of two winding configurations, as shown in Fig. 14(b). Therefore, on the balance of average thrust force and force fluctuations, machine with 12/7 is selected as prototype.
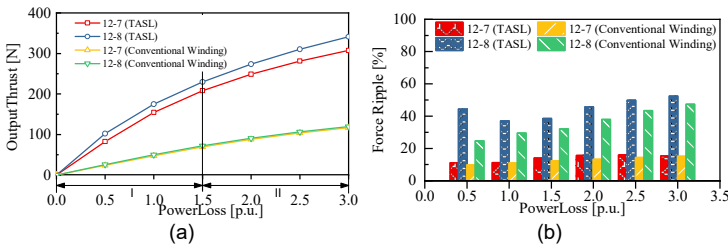

Fig. 14. Over-load capability of the proposed DS-DC-VRLM. *(a) The average force. (b) Thrust force ripple.*

D. Loss, and Efficiency Analysis

The copper loss of the motor has been fixed to 240W, and the iron loss of the motor can be calculated as (20) [20],

$$P_{Fe} = P_h + P_e + P_c = K_h f_e B_m^2 + K_e (f_e B_m)^{1.5} + K_c (f_e B_m)^2 \qquad (20)$$

where K_h is the hysteresis core loss coefficient, K_c is eddy effect coefficient, K_e is the excess coefficient, f_e is the electrical frequency, and B_m is the flux density in the core. The iron loss varies with velocity and B_m in the iron core.
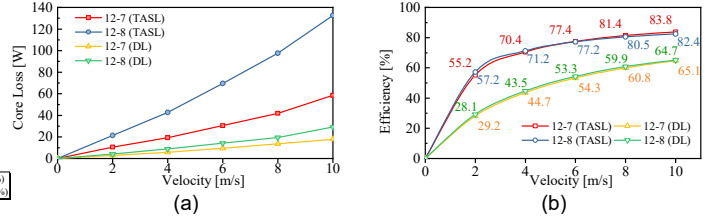

Fig. 15. Loss analysis of DS-DC-VRLM at different speed with copper loss 240W. *(a) core loss. (b) Efficiencies.*

Fig.15 presents the iron loss and efficiency of the linear motor at speed of 1m/s to 10m/s under rated power condition (240W). As shown in Fig. 15(a), due to the richer harmonics contents of TASL winding, the core loss is much higher than conventional winding. As the motor accelerates, the core loss of TASL winding increases quicker than conventional winding. As shown in Fig. 15(b), the efficiency of the proposed machine with 12/7 combination reaches 83.8% at speed of 10m/s, which is slightly higher than its 12/8 counterpart, which could be attributed to the higher iron loss caused by higher electrical frequency and easier saturation effect in the machine of 12/8 slot/pole combination.

E. Comparative Study

To furtherly illustrate the advantages of the proposed machine in output thrust force, the proposed machine is also compared with the other existing magnet-less machine, namely, 12-10 full-pitched variable flux reluctance linear machine (VF-RLM) with conventional toroidal winding [7], DC-exited flux switching linear machine (DCE-FSLM) [8] and switched reluctance linear machine (SRLM) under the same copper loss (240W), dimension and stack length for fair comparison. The topologies of these three machines are shown as following Fig. 16. As shown in Fig. 16(a), DC field winding of the VF-RLM is wound toroidally in every primary slot, and conventional toroidal single- layer winding is adopted for the armature winding. It is shown in Fig. 16(b), the DCE-FSLM adopts 12/7 slot/ pole combination, whose armature winding wound across two teeth. Meanwhile, SRLM with 12/8 slot/ pole combination is shown in Fig. 16(c), where conventional single-layer toroidal armature winding is adopted. The SRLM uses semi-period conduction (180° conduction angle control), while the other DC-excited machine adopts field-oriented vector control. The design parameters of the proposed machine are listed in the TABLE IX. As shown in TABLE IX, the VF-LRM could achieve lowest force ripple (3.76%) but also with the lowest output thrust force in average (67.34N). In comparison with DCE- FSLM, the proposed design could obtain approximately 17.94% higher thrust force with slightly lower thrust ripple ratio. As a matter of fact, DCE- FSLM and the proposed design have the same field excitation. By comparison, the proposed design has higher winding factor than conventional DCE- FSLM. SRLM with conventional single-layer toroidal armature winding could obtain basically same thrust force, but with much higher thrust ripple (107.87%).

Fig. 17 presents the overload capability of the proposed TASL winding and other three existing design. It is shown in Fig. 17 that the proposed winding configuration could further enhance

the overload capability and the maximum output thrust force is 307.42N for TASL, 287.48N for SRLM, 255.22N for DCE-FSLM, and 121.70N for VF-LRM and when the copper loss of the machine is tripled to the rated one. With the electrical load of the motor increase, the output thrust force of the VRLM with TASL winding could achieve basically same output thrust force in average as SRLM, but with much lower thrust ripple (12.04% under rated power). In comparison with conventional VF-LRM design, the proposed design could 153.7% higher output thrust, while the thrust force ripple is also much higher. On the other hand, comparing with existing DCE-FSLM, the proposed VRLM could obtain 20.39% higher thrust force, also the thrust ripple is also lower than existing DCE-FSLM.

TABLE IX DESIGN PARAMETERS AND PERFORMANCES COMPARISONS

|	VF-LRM	DCE-FSLM	SRLM	Proposed
L_m, Mover teeth length (mm)		210		
L_{stk}, Stack length (mm)		50		
F_f, Filling factor		0.45		
k_{sp}, Split ratio	0.75	0.70	0.70	0.70
k_{dc}, DC to total loss ratio	0.48	0.55	-	0.55
$P_{loss(cu)}$, copper loss (W)		240		
N_{ac}, Number of AC turns per coil	70	42	84	84
N_{dc}, Number of DC turns per coil	65	84	-	84
$i_{q(max)}$, Q-axis RMS Current (A)	7.07	8.71	11.33	8.71
i_{dc}, DC current (A)	7.00	9.70	-	9.70
f_t, Rated thrust force (N)	67.34	119.65	138.13	141.12
R_{rip}, Force ripple ratio (%)	3.76	16.71	107.87	12.04
D_t, Thrust force density(kN/m³)	80.17	142.44	164.45	168.00

(a)

(b)

(c)
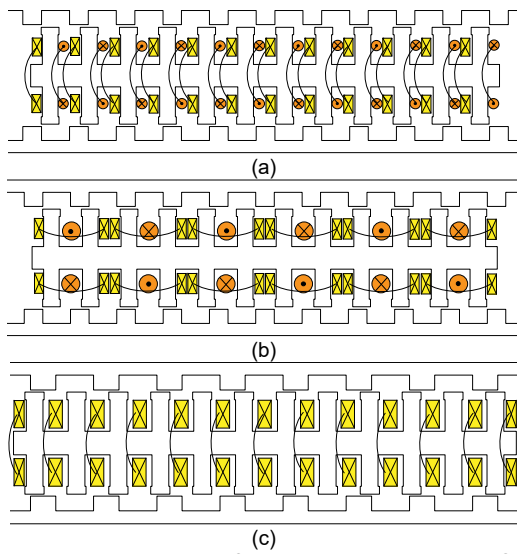
Fig. 16. Traditional winding configuration. *(a) VF-LRM (b) DCE-FSLM (c) Switched reluctance linear machine*
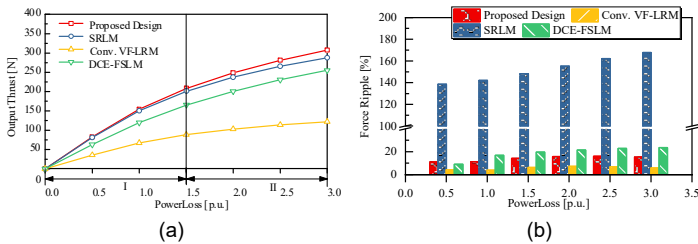

(a)

(b)

Fig. 17. Over-load capability of the proposed DS-DC-VRLM. *(a) The average force. (b) Thrust force ripple.*

V. EXPERIMENTAL VERIFICATION

To verify the feasibility of the proposed topology, the prototype is manufactured after the geometric parameters of 12/7 machine listed in TABLE VIII, which achieves lower thrust ripple and higher efficiency. DW540_50 is selected as the laminated iron of stator and mover. The rated speed is selected as 1m/s for the test. AWG 17 is selected for the copper wire.
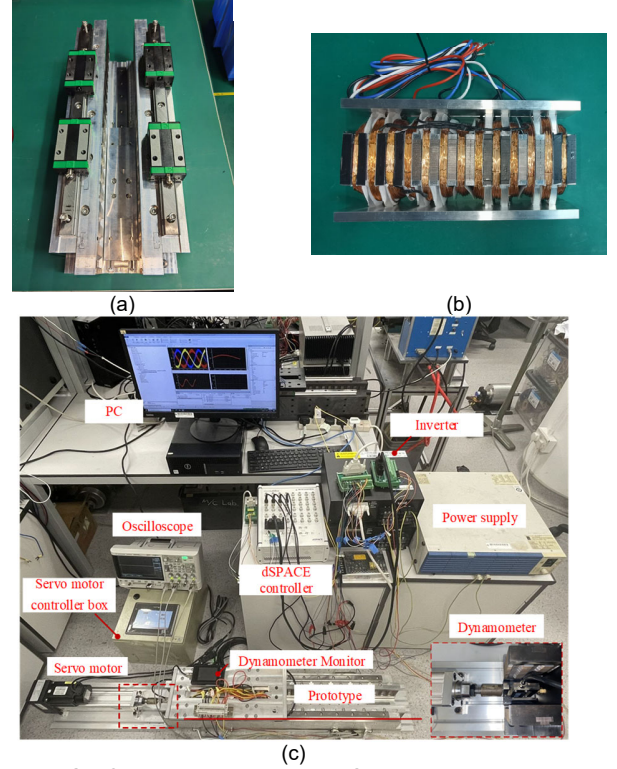

(a)

(b)

(c)

Fig. 18. DS-DC-VRLM prototype. *(a) Stator assembly. (b) Mover assembly. (c) Prototype and test platform.*
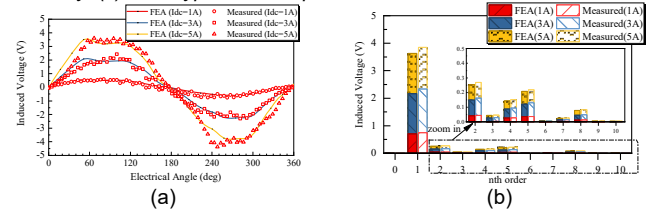

(a)

(b)

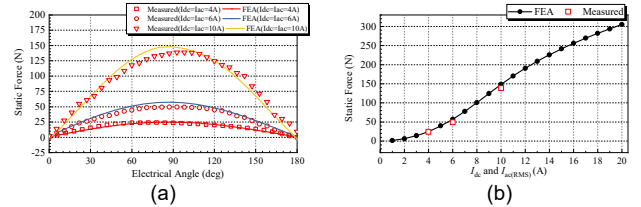Fig. 19. Induced voltage of phase A *(a) Waveform (b) Spectrum*

(a)

(b)

Fig. 20 On-load static test results. *(a) Power angle curve (b) Different current density.*

Fig. 18 presents some details of the prototype. Fig. 18(a) shows the long rail stator assembly of the machine. The mover assembly is shown in Fig.18 (b). As shown in Fig. 18(b), the toroidal windings are used, which simplify the winding process and shorten the ends of coil as well. Fig. 18(c) demonstrates the test platform, which mainly consists of a servo linear motor, dynamometer, oscilloscope, dSPACE controller, inverter, etc. Fig. 19 compares the FEA and test results of the open-circuit induced

voltage waveforms and spectra under the rated velocity of 1m/s, and DC current is set as 1A, 3A and 5A, respectively. The experimental results agree well with FEM results.

Fig. 20 (a) presents the on-load test results of the machine under different power angles, when excitation current I_{dc} and RMS value of AC current $I_{ac(RMS)}$ are set as 4A, 6A and 10A, which indicates light, medium, and heavy loads, respectively. The errors between FEA results and test results are mainly caused by the dynamometer when the pull force and push force are applied in sequence in a relatively short time interval, and these errors increase along with the loads increase. Fig. 20 (b) compares the FEA and test of thrust force under different currents (from 1A to 20A). The maximum current density of the measured force in the experiment is 10A/mm², whose thrust force has reached 138.8N. Meanwhile, the maximum current density of the simulated force in the FEA is 20A/mm², whose thrust force has reached 305.0N. In addition, the saturation point of the prototype is around 14A. According to the calculation results, good agreements are obtained. To be noticed, though higher thrust force could be achieved when I_{dc} is slightly larger than RMS value of AC current (k_{dc}=0.54), the prototype is tested under the same DC and RMS value of AC to simplify the experimental step.
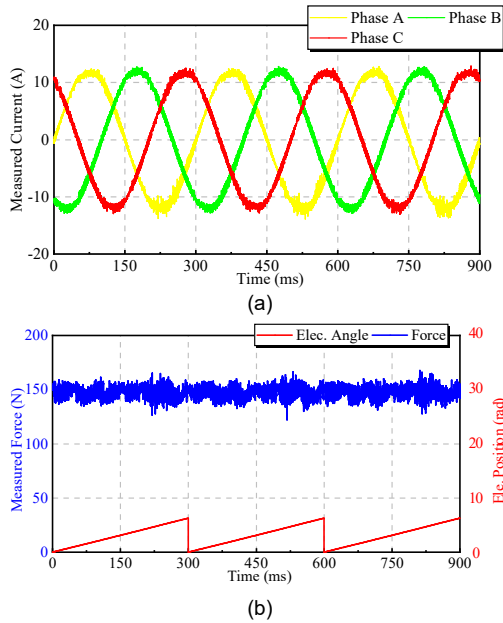

(a)

(b)

Fig. 21 On-load dynamic test results. *(a) Measured current. (b) Measured force and electrical angle position*

The dynamic test of the machine is conducted via closed-loop speed control based on primary field-oriented control (FOC). Fig. 21 presents the dynamic test of prototype using FOC algorithm, and the speed of the mover keeps 0.2m/s. As shown in Fig.21(a), following TABLE. VIII, the RMS value of the phase current is 10A, and DC current in the field winding is set as 10.13A, . Fig. 21(b) measured the force and the electrical angle of the machine, and it is shown that the thrust force of the machine in average is tested as 148.02N, and it is also tested that the thrust ripple of the machine is approximately 15.12%, which agrees with the calculation results of FEA method in Fig. 14 and TABLE VIII.

VI. CONCLUSION

In this paper, to further boost the thrust density of magnet-less linear machine, a novel toroidal alternative single layer winding configuration is proposed for DS-DC-VRLM, whose DC windings are wound every two primary teeth. The thrust density of the machine with proposed TASL winding is 2.26 times higher than that of the conventional winding, when using 12/7 slot/pole combination on the balance of average thrust force and force fluctuations. The key is that the proposed armature winding makes full use of working harmonics modulated by both the fundamental order and the third-order harmonics from DC windings, contributing to enhanced winding factor. According to the harmonics analysis, it has been revealed that the ratio between the amplitude of $|P_{dc} - N_s|$ component and that of $|3P_{dc} - N_s|$ component is only 1.92 indicating that the harmonic, modulated from 3rd -order harmonic, is abundant in the air-gap, and with higher gear ratio. Therefore, TASL designed following $PPN=|3P_{dc} - N_s|$ with enhanced winding factor could achieve higher induced voltage and output thrust than conventional winding. After global optimization, the performances of the two better slot/ pole combinations with different winding configurations are evaluated under the fixed copper loss which has proved that the TASL windings could obtain higher output thrust, but with relatively higher thrust ripple and iron loss. The efficiency using TASL windings are still higher than the conventional concentrated windings thanks to the much higher output thrust.

However, the drawback of this winding configuration for DC-VRLM is that some useless harmonics caused by end effect cannot be fully cancelled, which enlarges the thrust ripple of it. Aiming to the ripple issue, a variety of methods including skew, auxiliary end teeth and combination of segmental mover arrangement could be applied to suppress the force ripple of it in the next step.

REFERENCES

[1] I. Boldea, L. N. Tutelea, W. Xu, and M. Pucci, "Linear Electric Machines, Drives, and MAGLEVs: An Overview," IEEE Transactions on Industrial Electronics, vol. 65, no. 9, pp. 7504-7515, 2018.

[2] J. Faiz and A. Nematsaberi, "Linear electrical generator topologies for direct-drive marine wave energy conversion- an overview," IET Renewable Power Generation, vol. 11, no. 9, pp. 1163-1176, Jul 2017.

[3] G. Stumberger, B. Stumberger, and D. Dolinar, "Identification of linear synchronous reluctance motor parameters," IEEE transactions on industry applications, vol. 40, no. 5, pp. 1317-1324, 2004.

[4] D. Wang, Z. Feng, H. Zheng, and X. Wang, "Comparative Analysis of Different Topologies of Linear Switched Reluctance Motor with Segmented Secondary for Vertical Actuation Systems," IEEE Transactions on Energy Conversion, 2021.

[5] X. Li, X. Wang, and S. Yu, "Design and Analysis of a Novel Transverse-Flux Tubular Linear Switched Reluctance Machine for Minimizing Force Ripple," IEEE Transactions on Transportation Electrification, vol. 7, no. 2, pp. 741-753, 2021.

[6] Y. Shen, Z. Zeng, Q. Lu, and Y. Li, "Investigation of a Modular Linear Doubly Salient Machine With Dual-PM in Primary Yoke and Slot Openings," IEEE Transactions on Magnetics, vol. 55, no. 6, pp. 1-6, 2019.

[7] T. W. Ching, Y. Shi, W. Li, and L. Jian, "Design and Analysis of a Magnetless Linear Variable Reluctance Motor With Modular Mover Units for Electric Propulsion," IEEE Transactions on Applied Superconductivity, vol. 30, no. 4, pp. 1-5, 2020.

[8] W. L. Li, K. T. Chau, C. H. Liu, and C. Qiu, "Design and Analysis of a Flux-Controllable Linear Variable Reluctance Machine," IEEE Transactions on Applied Superconductivity, vol. 24, no. 3, Jun 2014, Art. no. 5200604.

[9] Y. Shen and Q. Lu, "Investigation of Novel Multi-Tooth Linear Variable Flux Reluctance Machines," IEEE Transactions on Magnetics, vol. 54, no. 11, pp. 1-5, 2018.

[10] X. Zhao, S. Niu, and W. Fu, "A New Modular Relieving-DC-Saturation Vernier Reluctance Machine Excited by Zero-Sequence Current for Electric Vehicle," IEEE Transactions on Magnetics, vol. 55, no. 7, pp. 1-5, 2019.

[11] X. Zhao and S. Niu, "Design of a Novel Parallel-Hybrid-Excited Vernier Reluctance Machine with Improved Utilization of Redundant Winding Harmonics," IEEE Transactions on Industrial Electronics, vol. 65, no. 11, pp. 9056-9067, 2018.

[12] S. Jia, R. Qu, J. Li, D. Li, and H. Lu, "Comparison of Stator DC Current Excited Vernier Reluctance Machines with Different Field Winding Configurations," IEEE Transactions on Magnetics, vol. 53, no. 6, pp. 1-4, 2017.

[13] S. Jia, R. Qu, J. Li, and D. Li, "Principles of Stator DC Winding Excited Vernier Reluctance Machines," IEEE Transactions on Energy Conversion, vol. 31, no. 3, pp. 935-946, 2016.

[14] X. Zhao, S. Wang, S. Niu, W. Fu, and X. J. I. T. o. I. E. Zhang, "A novel high-order-harmonic winding design method for vernier reluctance machine with DC coils across two stator teeth," 2021.

[15] Y. Du, C. Zhang, X. Zhu, et al., "Principle and analysis of doubly salient PM motor with π-shaped stator iron core segments", IEEE Trans. Ind. Electron., vol. 66, no. 3, pp. 1962-1972, Mar. 2019.

[16] D. Wang, X. Du, D. Zhang, and X. Wang, "Design, Optimization, and Prototyping of Segmental-Type Linear Switched-Reluctance Motor With a Toroidally Wound Mover for Vertical Propulsion Application," IEEE Transactions on Industrial Electronics, vol. 65, no. 2, pp. 1865-1874, 2018.

[17] B. Ullah, F. Khan, S. Hussain, and B. Khan, "Modelling, Optimization and Analysis of Segmented Stator Flux Switching Linear Hybrid Excited Machine for Electric Power Train," IEEE Transactions on Transportation Electrification, 2022.

[18] H. Zhang, B. Kou, Z. Q. Zhu, R. Qu, J. Luo, and Y. Shao, "Thrust Ripple Analysis on Toroidal-Winding Linear Permanent Magnet Vernier Machine," IEEE Transactions on Industrial Electronics, vol. 65, no. 12, pp. 9853-9862, 2018.

[19] M. Jiang, W. Fu, and S. Niu, "Design and Analysis of a Novel Dual-Airgap Dual Permanent Magnet Vernier Machine," IEEE Access, vol. 9, pp. 57188-57197, 2021.

[20] J. Ou, Y. Liu, M. Schiefer, and M. Doppelbauer, "A Novel PM-Free High-Speed Linear Machine With Amorphous Primary Core," IEEE Transactions on Magnetics, vol. 53, no. 11, pp. 1-8, 2017.

[21] G. Q. Ming, L. J. Wu and L. Zhang, "A Novel DC-Excited Doubly Salient Machine with Modular II-Shaped Stator Iron Core," 2020 International Conference on Electrical Machines (ICEM), 2020, pp. 33-38, doi: 10.1109/ICEM49940.2020.9270941.

Zhenghao Li received the B.Sc. degree in electrical engineering from South China University of Technology, Guangzhou, China, in 2016, the M.Sc. degree from University of Chinese Academy of Sciences, Beijing, China, in 2019, and he is currently working toward the Ph.D. degree with the Department of Electrical Engineering, Hong Kong Polytechnic University, Hong Kong. His research interests include design of novel linear machine.

Xing Zhao received his B. Eng. degree from Nanjing University of Aeronautics and Astronautics, China, in 2014, and then obtained Ph.D. degree from The Hong Kong Polytechnic University, Hong Kong SAR, in 2020, both in Electrical Engineering. Since Nov. 2021, he has been a Lecturer in Electrical Engineering in the Department of Electronic Engineering of University of York, UK. His research interests involve electrical machines and drives.

SHUANGXIA NIU received the B.Sc. and M.Sc. degrees in electrical engineering from Tianjin University, China, in 2002 and 2005, respectively, and the Ph.D. degree from The University of Hong Kong, Hong Kong, in 2009. She is currently an Associate Professor with the Department of Electrical Engineering, The Hong Kong Polytechnic University, Hong Kong. Her research interests include electrical machines and renewable energy conversion.